

Hysteretic electronic phase transitions in correlated charge density wave state of 1T-TaS₂Yanyan Geng,^{1,2} Le Lei,^{1,2,3} Haoyu Dong,^{1,2} Jianfeng Guo,^{1,2} Shuo Mi,^{1,2} Yan Li^{①,3}, Li Huang,³ Fei Pang,^{1,2} Rui Xu,^{1,2} Weichang Zhou,⁴ Zheng Liu^{①,5}, Wei Ji^{①,2,*} and Zhihai Cheng^{①,2,†}¹*Beijing Key Laboratory of Optoelectronic Functional Materials & Micro-nano Devices, Department of Physics, Renmin University of China, Beijing 100872, People's Republic of China*²*Key Laboratory of Quantum State Construction and Manipulation (Ministry of Education), Renmin University of China, Beijing, 100872, People's Republic of China*³*Beijing National Laboratory for Condensed Matter Physics, Institute of Physics, Chinese Academy of Sciences, Beijing 100190, People's Republic of China*⁴*Key Laboratory of Low-Dimensional Quantum Structures and Quantum Control of Ministry of Education, College of Physics and Information Science, Hunan Normal University, Changsha 410081, People's Republic of China*⁵*Institute for Advanced Study, Tsinghua University, Beijing 100084, People's Republic of China*

(Received 9 December 2022; revised 19 April 2023; accepted 19 April 2023; published 2 May 2023)

The layered transition metal dichalcogenide 1T-TaS₂ has evoked great interest owing to its particularly rich electronic phase diagram including different charge density wave (CDW) phases. However, few studies have focused on its hysteretic electronic phase transitions based on the in-depth discussion of the delicate interplay among temperature-dependent electronic interactions. Here, we report a sequence of spatial electronic phase transitions in the hysteresis temperature range (160–230 K) of 1T-TaS₂ via variable-temperature scanning tunneling microscopy. Several emergent electronic states are investigated at multiscale during the commensurate CDW–triclinic CDW (CCDW–TCDW) phase transitions: a spotty-CDW state above ~160 K, a network-CDW (NCDW) state above ~180 K during the warmup process, a belt-TCDW state below ~230 K, a NCDW state below ~200 K, and finally a mosaic-CDW state below ~160 K during cooldown from the TCDW phase. These emergent electronic states are associated with the delicate temperature-dependent competition and/or cooperation of stacking-dependent interlayer interactions, intralayer electron-electron correlations, and electron-phonon (*e-ph*) coupling of 1T-TaS₂. Our results not only provide insight to understand the hysteretic electronic phase transitions in the correlated CDW state, but also pave a way to realize more exotic quantum states by accurately and effectively tuning various interior interactions in correlated materials.

DOI: [10.1103/PhysRevB.107.195401](https://doi.org/10.1103/PhysRevB.107.195401)**I. INTRODUCTION**

Low-dimensional materials can exhibit various intriguing electronic ordering states, including charge density wave (CDW), spin density wave (SDW), superconductivity (SC), electronic nematicity, and so on [1–3]. As an archetype charge-ordered state, the CDW state normally consists of a periodic modulation of the electronic charge density accompanied by a periodic distortion of the atomic lattice [4,5]. The most commonly considered mechanisms for the formation of conventional CDW states are related to a Fermi surface nesting and electron-phonon (*e-ph*) coupling [6,7]. A series of complicated CDW states have triggered off tremendous research interest in two-dimensional transition metal dichalcogenide (TMD) materials, such as 2H-NbSe₂ (3 × 3 CDW) [8,9], 2H-TaSe₂ (3 × 3 CDW) [8], 1T-TiSe₂ (2 × 2 CDW) [10], 1T-TaSe₂ ($\sqrt{13} \times \sqrt{13}$ CDW) [11,12], and monolayer VSe₂ ($\sqrt{7} \times \sqrt{3}$ CDW) [8]. More exotic electronic states, including SC [13], Anderson insulator [14], and normal metal [14], can be further induced in these TMD

materials by effectively controlling the CDW states through external pressure [15], element doping [16], interlayer intercalation [17], etc.

The bulk 1T-TaS₂ is a well-known CDW material with a sequence of phase transitions with decreasing temperatures: from a metallic incommensurate CDW (ICCDW) phase, through a nearly commensurate CDW (NCCDW) phase, to a correlated commensurate CDW (CCDW) phase [5,18]. The correlated CCDW phase has attracted extensive attention due to the complex electron-electron correlation effect and possible existence of a quantum spin liquid (QSL) state [19]. It was previously assumed that the ground CCDW state of 1T-TaS₂ is driven by the single-band Mott-Hubbard mechanism [20], whereas the stacking-dependent interlayer interactions have recently been emphasized as having an indispensable role in understanding the insulating mechanism of 1T-TaS₂. Recent scanning tunneling microscopy (STM) and angle-resolved photoemission spectroscopy (ARPES) measurements have given some robust evidence of dimerization along the *c* axis, and simplified the insulating state into a trivial band insulator [21–24].

At low temperatures, the precise site-specific scanning tunneling spectroscopy (STS) measurements [21,24] have been used to directly distinguish the Mott- or band-insulating

* wji@ruc.edu.cn

† zhihaicheng@ruc.edu.cn

regions on the surface of $1T$ -TaS₂. At high temperatures, the temperature-dependent ARPES measurements indicated a distinctive electronic phase transition from the band insulator with interlayer dimerization gradually to the Mott insulator without interlayer stacking order within the CCDW-TCDW (triclinic CDW) hysteresis temperature range [25]. Such electronic phase transition with the decoupling of the interlayer stacking order can not only be triggered by changes in temperature but also by means of strain/pressure, interlayer intercalation, and element substitution [18–20]. To deeply understand and effectively control this electronic phase transition of $1T$ -TaS₂, it is necessary to study the competition of stacking-dependent interlayer interactions and intralayer interactions in detail, and for any tunable interactions of $1T$ -TaS₂, the evolution of the electronic phase transition itself becomes of great importance. Making a deep investigation of CCDW-TCDW hysteretic phase transition and observing the spatial variation in the correlated CDW state may contribute to a further in-depth understanding of the temperature-dependent various interactions of $1T$ -TaS₂.

In this paper, the CCDW-TCDW hysteretic phase transitions of $1T$ -TaS₂ were reported in real space by variable-temperature STM (VTSTM). The emergence, evolution, coexistence, and separation of diverse electronic states within the CCDW/TCDW phase are investigated at multiscale (from the atomic scale to mesoscopic scale) through the warmup/cooldown process. These emergent electronic states can be phenomenologically attributed to the competition and/or cooperation of stacking-dependent interlayer interactions, intralayer electron-electron correlation, and e - ph coupling of $1T$ -TaS₂.

II. RESULTS

As shown in Fig. 1(a), $1T$ -TaS₂ exhibits a CdI₂-type layered crystal structure with Ta atoms octahedrally coordinated by S atoms. At low temperatures, strong e - ph coupling induced periodic lattice distortion makes a perfect $\sqrt{13} \times \sqrt{13}$ superlattice in the ground CCDW state [20], in which every 13 Ta atoms are distorted to form the Star of David (SD) clusters, as shown in Figs. 1(b) and 1(c). Each SD cluster contains 13 Ta $5d$ electrons, the 12 electrons of the outer Ta atoms pair and form six occupied insulating bands, and leave one unpaired electron (Mott) of the central Ta atom in a half-filled metallic band [20,26]. The strong intralayer electron-electron correlations introduce a Mott gap of about 0.2–0.4 eV at low temperatures, forming a correlated Mott insulator without considering the interlayer interactions [21]. Recently, the important role of the interlayer stacking order has been emphasized, and the ground CCDW state of $1T$ -TaS₂ can be described as a trivial band insulator/conventional Mott insulator on the termination of T_A/T_C stacking at low temperatures [21,24]. Intriguingly, these stacking-sensitive interlayer interactions not only play a dominant role in the ground CCDW state, but also have a significant effect on the electronic phase transitions in the correlated CDW state of $1T$ -TaS₂, particularly the CCDW-TCDW phase transition.

As shown in Fig. 1(d), the bulk $1T$ -TaS₂ undergoes a series of CDW transitions with prominent hysteretic behavior at ~ 200 K. During the cooldown process, $1T$ -TaS₂

directly transforms from the NCCDW phase into the CCDW phase at ~ 180 K with persistent threefold rotation symmetry. However, during the warmup process, $1T$ -TaS₂ undergoes a relatively complex CDW transition from the threefold symmetric CCDW phase to the stripelike nematic TCDW phase at ~ 220 K. Subsequently, the $1T$ -TaS₂ enters an NCCDW phase at ~ 280 K with hexagonal CCDW domains in discrete distribution. These localized CCDW domains shrink upon warmup and finally disappear at ~ 350 K, when the system enters a metallic ICCDW phase. In the above phase transitions, although most previous studies have been extensively focused on the CCDW-NCCDW phase transition [27–29], we mainly focus on the spatial CCDW-TCDW phase transitions owing to the more delicate competition of various interactions of $1T$ -TaS₂.

The schematic in Fig. 1(e) illustrates the delicate interplay of the interlayer and intralayer interactions during the CCDW-TCDW phase transition of $1T$ -TaS₂. The low-temperature CCDW state is primarily governed by strong interlayer interactions with the stable stacking order rather than intralayer electron-electron correlations [22,23]. As the temperature increases, the interlayer stacking order is gradually random with many unstable stacking interfaces [22]. Meanwhile, the intralayer electron-electron correlations gradually have a significant effect on correlated CDW states. At temperatures above ~ 200 K, the interlayer stacking order completely vanishes and the intralayer electron-electron correlations play a more dominating role than the stacking-dependent interlayer interaction [25]. In addition, the warmup process is also accompanied by the weakening of e - ph coupling and relative enhancement of in-plane electron hopping [7]. At temperatures above ~ 230 K, the delicate interplay of the e - ph coupling and electron-electron correlations induces the emergence of the TCDW phase. This temperature-dependent competition between the interlayer and intralayer interactions can induce diverse spatially distributed exotic electronic states in the CCDW-TCDW phase transition range of $1T$ -TaS₂.

At temperatures above ~ 160 K, randomly distributed bright clusters first emerge within the CCDW phase, as shown in Figs. 2(a) and 2(b); this is referred to as the spotty-CDW (SCDW) state. These bright clusters normally consist of approximately —five to eight bright SDs and account for $\sim 20\%$ of the entire SCDW state. The apparent heights of the bright clusters are ~ 50 pm higher than that of the remaining pristine SDs of the SCDW state (Appendix A). The local electronic states of the bright clusters (red dot) and pristine SD regions (blue dot) of the SCDW state are further determined through site-specific STS spectroscopy measurements, as shown in Fig. 2(c). For the pristine SD regions, the small gap of ~ 50 mV can be clearly identified even at the temperature of ~ 160 K, whereas the bright clusters exhibit a V-shaped feature with no gap. We suppose that the V-shaped metallic nature of the bright clusters may be associated with the delocalization of Mott electrons, which exhibit behavior from localized to itinerant at the bright cluster.

Figures 2(d)–2(f) show a further emergent bright stripe network within the SCDW state at temperatures above ~ 180 K. The mesoscopic bright stripe network consists of bright clusters and the long bright stripes connected via the “Y shape,” “X shape,” and “loop shape,” as shown in Fig. 2(d), which is

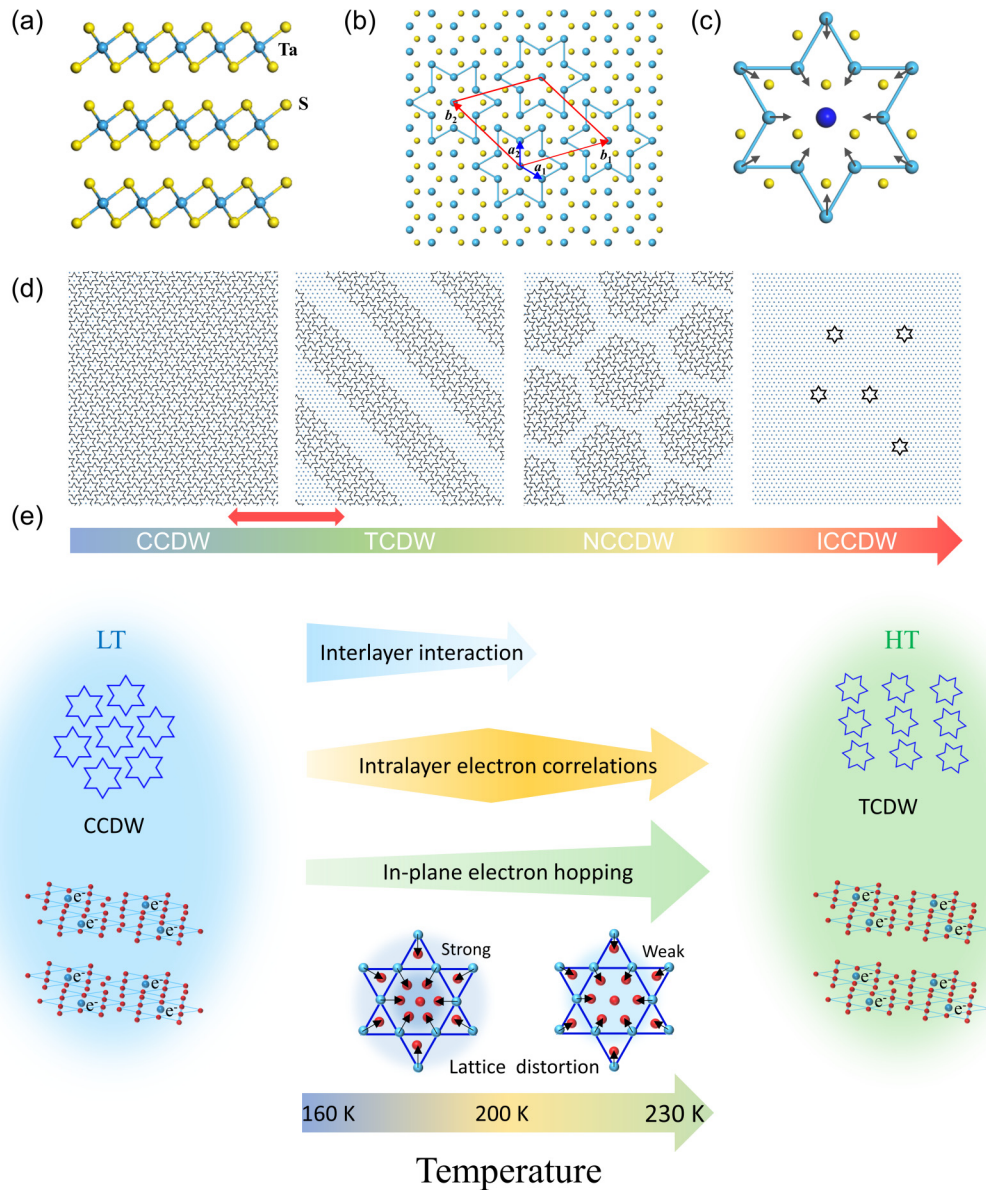


FIG. 1. Atomic structure and correlated CDW states of $1T$ - TaS_2 . (a) Atomic crystal structure of the bulk $1T$ - TaS_2 . (b) Schematic of the ground CCDW state of monolayer $1T$ - TaS_2 with a $\sqrt{13} \times \sqrt{13}$ superlattice. b_1 and b_2 are the basis vectors of the CCDW superlattice, whereas a_1 and a_2 are the basis vectors of the underlying atomic lattice. (c) Schematic of the structure of the Star of David (SD) unit in the CCDW state. The gray arrows indicate that the 12 surrounding Ta atoms shrink to the central Ta (blue) atom. (d) Schematics of the sequential CCDW, TCDW, NCCDW, and ICCDW phases during the warmup process. The SD clusters are marked with dark stars. The red double arrow indicates the CCDW-TCDW hysteretic phase transition intervals that this paper focuses on. (e) Schematic of the delicate interplay of the complex interlayer and intralayer interactions during the warmup CCDW-TCDW phase transition of $1T$ - TaS_2 . The three colored arrows indicate the three main interactions including interlayer interaction, intralayer electron correlations, and in-plane electron hopping of $1T$ - TaS_2 . The change in the width of the arrows indicates the relative change between the three interactions during the warmup process, and the width indicates which interaction dominates at which temperature.

called the network-CDW (NCDW) state. In the NCDW state, SCDW domains with various sizes and shapes are separated by the bright stripe network, as shown in Fig. 2(e). The bright stripes can also be assumed as the domain walls between the neighboring SCDW domains as shown in Fig. 2(f), which are similar to the incommensurate areas of the TCDW/NCCDW phase.

We suggest that the spontaneous emergence of bright clusters and bright stripes at temperatures above ~ 160 K

is associated with the vanishing of the interlayer stacking order and the dominance of electron-electron correlations. Compared with the stable local bright clusters, the global bright stripe network is relatively unstable with various dynamic behaviors, including breaking, shrinking, and disappearing, as shown in Appendix A. The isolated stripe loops can be decomposed from the global bright stripe network, indicating their specific topological stability. The dynamic characteristics of the bright stripes may origi-

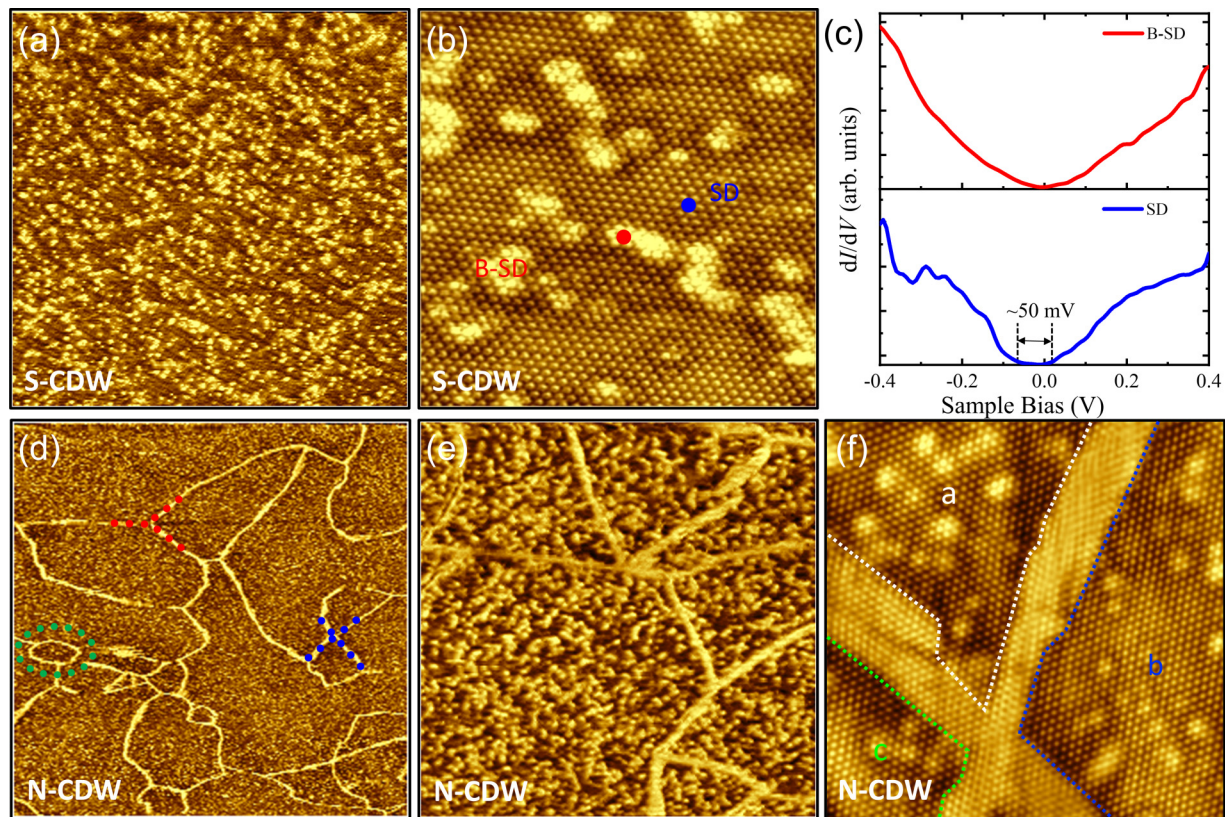


FIG. 2. Emergent spotty-CDW (SCDW) and network-CDW (NCDW) electronic states within the CCDW phase during the warmup process. (a) Large-scale STM image of the CCDW phase with the emergent distributed bright clusters, which is called the SCDW state. (b) High-resolution STM image of the SCDW state. (c) Site-specific STM dI/dV spectroscopy performed at the bright clusters and SDs of the SCDW state marked in (b). The small gap ~ 50 mV in the SD region is clearly identified, while the bright clusters (B-SD) exhibit a V-shaped feature with no gap. (d) Mesoscopic-scale STM image of the CCDW phase with the emergent distributed bright clusters and bright stripe network, which is called the NCDW state. The network consists of bright stripes connected via the “Y-shape” (red), “X shape” (blue), and “loop shape” (green). (e) Large-scale STM image of the NCDW state. (f) High-resolution STM image of the NCDW state. The different SCDW domains [marked by (a)–(c)] are separated by the bright stripe network. Imaging parameters: $0.25 \times 0.25 \text{ } \mu\text{m}^2$ (a); $50 \times 50 \text{ nm}^2$ (b); $1.5 \times 1.5 \text{ } \mu\text{m}^2$ (d); $0.15 \times 0.15 \text{ } \mu\text{m}^2$ (e); $75 \times 75 \text{ nm}^2$ (f). $V_b = 200 \text{ mV}$, $I_t = 100 \text{ pA}$ (a)–(f).

nate from the instability of the CDW caused by the e - ph coupling.

At temperatures above ~ 230 K, a stripelike TCDW phase is observed, as shown in Fig. 3(a). The TCDW phase is composed of the bright stripes of enhanced CDW maxima (CCDW), separated by dark stripes of diminished CDW amplitude (ICCDW) as shown in Fig. 3(b). The stripes distribute along the high-symmetry directions of the underlying atomic lattice, showing an exotic spontaneously broken rotational symmetry relative to the low-temperature hexagonal CCDW phase. The topographic line profile of Fig. 3(c) is measured along the dashed line in Fig. 3(b), indicating a rough ratio, 2:3, of ICCDW and CCDW stripes. The average periodicity of the TCDW phase can be quantitatively determined via the fast Fourier transform (FFT) of its large-scale STM images, as shown in Fig. 3(d). The stripelike and hexagonal arrangements of the SDs in the TCDW phase are represented by the satellite and main FFT spots, marked by the small orange and large green circles, respectively, in Fig. 3(d). The averaged periodicity of the TCDW phase can be determined

as five SDs by the relative ratio of red and green arrows, i.e., 1:5.

At temperatures above ~ 280 K, the well-known NCCDW phase emerged from the stripelike TCDW phase with the reappeared threefold rotational symmetry, as shown in Fig. 3(e). The NCCDW phase consists of the hexagonal array of CCDW domains separated by the connected ICCDW network. The averaged periodicity of the NCCDW phase can be quantitatively determined by its FFT in Fig. 3(f), where the hexagonal arrangements of the CCDW domains and SDs are represented by the satellite and main FFT spots, respectively. The rough periodicity (2:5) of the CCDW domain superlattice is further determined by the length ratio (1:7) of the blue and green vectors.

The phase transition of CCDW-TCDW/NCCDW is widely considered to be a first-order phase transition; these first-order phase transitions are often driven by the intralayer electron-electron correlations and e - ph coupling [5,18]. In the TCDW phase and NCCDW phase, domains of SD clusters are isolated from each other by a metallic network (domain wall);

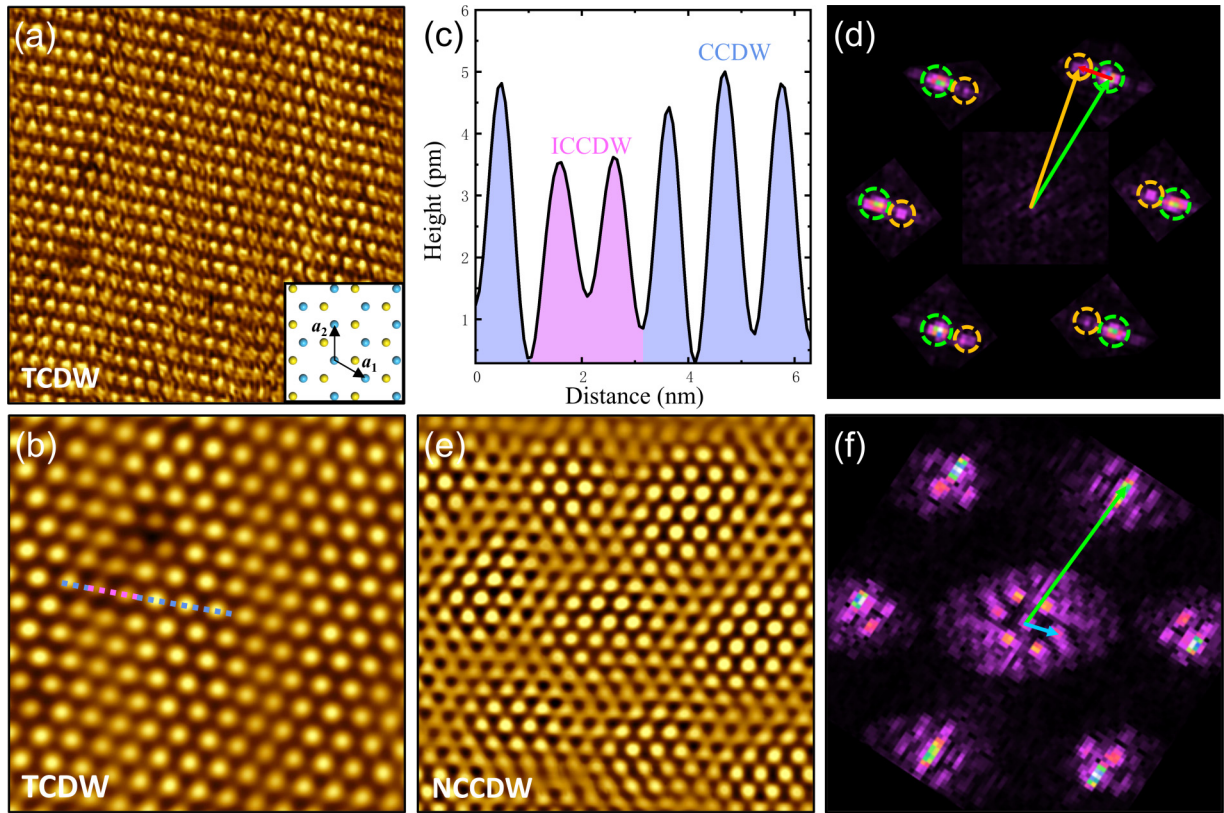


FIG. 3. STM measurements of the TCDW and NCCDW phases of $1T$ -TaS₂ at temperatures above ~ 230 K. (a) Large-scale STM image of the stripelike TCDW phase. The stripes are arranged in the high-symmetric directions of the underlying atomic lattice. The inset shows the basis vectors of the underlying atomic lattice. (b) High-resolution STM image of the CCDW and ICCDW stripes in the TCDW phase. (c) Topographic line profile along the dashed line in (b), showing the rough periods of ICCDW and CCDW stripes. (d) Fast Fourier transform (FFT) pattern of the TCDW phase. The green (red) arrows indicate the periodical stripelike arrangements of CDW/ICCDW domains (hexagonal arrangements of SDs) in the TCDW phase. (e) High-resolution STM image of the NCCDW phase. (f) FFT of (e). The blue (green) arrows indicate the hexagonal arrangements of CCDW domains (SDs) in the NCCDW phase, respectively. Imaging parameters: 40×40 nm², $V_b = 100$ mV, $I_t = 150$ pA (a); 25×25 nm², $V_b = 100$ mV, $I_t = 150$ pA (b); 20×20 nm², $V_b = 100$ mV, $I_t = 150$ pA (e).

the reorientation of the Ta atoms of the domain wall can be attributed to the e - ph coupling of $1T$ -TaS₂ [31]. The nematic TCDW and hexatic NCCDW phases can be explained by the interplay of intralayer electron-electron correlations and e - ph coupling.

Direct cooldown from the stripelike TCDW phase and the transition from the TCDW phase to the CCDW phase are investigated as shown in Fig. 4, while the previous work mainly focused on the NCCDW-CCDW transition [27–29]. Figure 4(a) shows a typical mesoscopic-scale STM image of the bright belts that emerged through the split-decomposition process from the TCDW phase, which is named the belt-TCDW (BTCDW) state. The detailed formation process of the BTCDW state is shown in Appendix B. The zoomed-in STM image of the BTCDW region with the dense bright belts (the initial stage of the BTCDW state) is shown in Fig. 4(b). These bright belts are arranged in parallel at fixed intervals along the atomic lattice direction; the orientation of the bright belts reflects the e - ph coupling and the distance of the bright belts reflects the electron-electron correlations. We suggest

that the competition of electron-electron correlations and e - ph coupling in $1T$ -TaS₂ is responsible for the BTCDW state.

The SCDW state with bright clusters reappeared between the bright TCDW belts. The rough periodicity and width of the parallel belts are estimated to be ~ 70 and ~ 35 nm, respectively, according to the topographic line profile of Fig. 4(c). Large-scale and atomic-scale STM images of the further decomposed BTCDW state are shown in Figs. 4(d) and 4(e), respectively. The shrinking widths and rugged edges of the TCDW belts in Fig. 4(d) indicate that the reappearance of bright clusters is caused by the further decomposition of the TCDW belts. The interval CCDW and ICCDW stripes are still observed in the TCDW belts, as shown in Fig. 4(e), suggesting that the two coexisting characteristic lengths of ~ 6 nm (TCDW) and ~ 70 nm (BTCDW) play significant roles at the atomic scale and mesoscopic scale, respectively, during the entire split-decomposing process of the TCDW phase. We attribute these characteristic lengths to the delicate competition between the electron-electron correlations and e - ph coupling interaction.

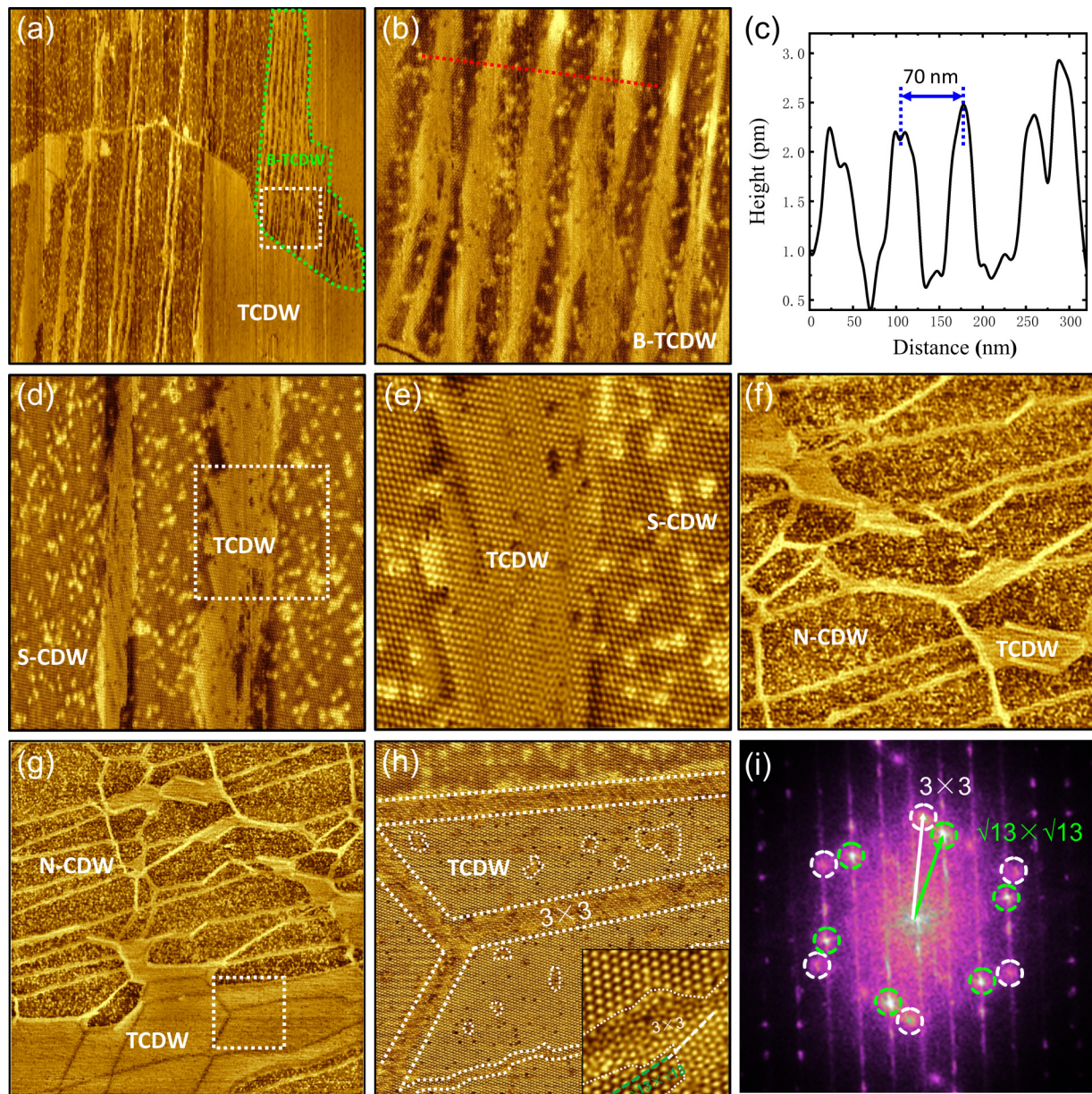


FIG. 4. Emergent belt-TCDW (BTCDW) and NCDW electronic states within the TCDW phase during cooldown process from ~ 230 K. (a) Mesoscopic-scale STM image of the parallel TCDW belts, which is called the BTCDW state. The TCDW area that has undergone a phase transition exhibits a striped pattern. The initial stage of the BTCDW state decomposed from the TCDW phase highlighted by the green dashed line. (b) High-resolution STM image of the BTCDW state. (c) Topographic line profile measured along the red line in (b). The rough periodicity and width of the parallel belts are estimated as ~ 70 and ~ 35 nm, respectively. (d), (e) Large-scale and atomic-scale STM images of the TCDW belts; (e) shows a zoomed-in STM image of the area marked by the white dashed square in (d). (f), (g) Mesoscopic-scale STM image of the NCDW state with the residual TCDW regions. (g), (h) Mesoscopic-scale and high-resolution STM images of the emergent 3×3 CDW state within the residual TCDW regions, appearing as the connected dark stripes marked by the dotted lines. Inset shows the clearly 3×3 CDW structure. (i) FFT pattern of (h). The emergent 3×3 and pristine $\sqrt{13} \times \sqrt{13}$ CDW superlattices are marked by white and green circles, respectively. The streaks in the FFT include all the $\sqrt{13} \times \sqrt{13}$ CDW peaks, which may be related to the residual TCDW phase. Imaging parameters: $1.5 \times 1.5 \text{ } \mu\text{m}^2$ (a); $300 \times 300 \text{ nm}^2$ (b); $150 \times 150 \text{ nm}^2$ (d); $50 \times 50 \text{ nm}^2$ (e); $500 \times 500 \text{ nm}^2$ (f); $1.0 \times 1.0 \text{ } \mu\text{m}^2$ (h); $70 \times 70 \text{ nm}^2$ (i). $V_b = 200 \text{ mV}$, $I_t = 100 \text{ pA}$ (a)–(i).

At temperatures below ~ 200 K, a similar NCDW state reemerged, with a few small residual TCDW regions. It can be seen that all the residual TCDW domains having the same orientation at both the mesoscopic and atomic scales, as shown in

Fig. 4(f). Surprisingly, some unexpected dark stripes are observed within the residual TCDW regions in Fig. 4(g), and are clearly resolved as an emergent 3×3 CDW structure, marked by the white dotted lines in Fig. 4(h). As shown in Fig. 4(i),

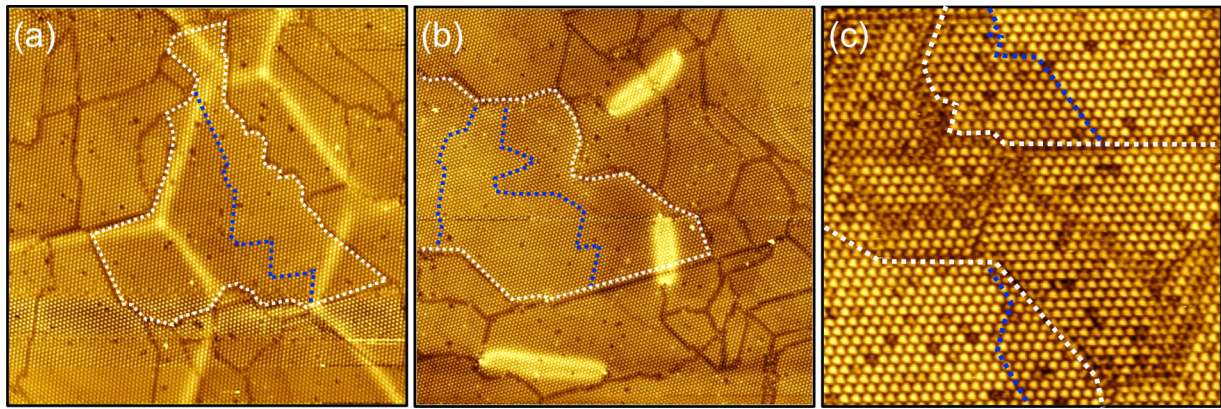


FIG. 5. Emergent mosaic-CDW (MCDW) state from the NCDW state during further cooldown process from ~ 160 K. (a), (b) Large-scale STM image of the MCDW state with various stacking orders. The residual bright stripes can still be observed. (c) High-resolution STM image of the MCDW state. Imaging parameters: $120 \times 120 \text{ nm}^2$. $V_b = 400 \text{ mV}$, $I_t = 150 \text{ pA}$ (a); $120 \times 120 \text{ nm}^2$. $V_b = 400 \text{ mV}$, $I_t = 150 \text{ pA}$ (b); $40 \times 40 \text{ nm}^2$. $V_b = 100 \text{ mV}$, $I_t = 150 \text{ pA}$ (c).

two different CDW vectors are clearly identified, shown by the white and green arrows, respectively, and the green arrows indicate the $\sqrt{13} \times \sqrt{13}$ CDW vectors. The angle between the white arrows and the green arrows is $\sim 13.9^\circ$ and the length ratio of the two lattice vectors is further measured to be about 1:0.86, which is approximately $\sqrt{13}:3$. Therefore the white wave vector can be determined to the 3×3 CDW structure. Recently, a similar 3×3 CDW structure has also been observed on the water-covered $1T$ -TaS₂ surface, which can be explained by the shifting of the phonon softening mode [30]. Since the momentum-dependent electron-phonon interactions are essential for the formation of CDW in TMDs, we suggest that the emergence of 3×3 CDW structures can be phenomenologically attributed to the modified e - ph coupling by the electron-electron correlations at the temperature of ~ 200 K. This 3×3 CDW structure needs to be investigated in depth in combination with theoretical calculations, which is beyond the scope of this paper. The more detailed underlying mechanisms of the 3×3 CDW structure will be discussed in our future work.

At temperatures below ~ 160 K, the NCDW state completely transforms into the global mosaic-CDW (MCDW) state with a few residual bright stripes, as shown in Figs. 5(a) and 5(b). The global MCDW state consists of irregularly distributed nanosized CCDW domains separated by well-defined domain wall textures [32,33], obviously different from the perfect CCDW state via direct cooldown from the NCCDW states [34]. Within the large CCDW domains of the surface layer (marked by white dashed lines), the two apparent heights can be faintly distinguished and separated by the marked blue lines. These different apparent heights in the surface layer sensitively depend on the specific stacking orders of the sublayers, and the domain wall existing in the sublayer(s) can also be visualized within the surface CCDW domains, as indicated by the blue lines in Figs. 5(a)–5(c).

III. DISCUSSION

The bulk $1T$ -TaS₂ undergoes a series of spatial electronic phase transitions during the warmup/cooldown process. In the

above phase transitions, we focus on the CCDW-TCDW hysteretic phase transitions, although most previous studies have focused on the CCDW-NCCDW phase transitions [27–29]. As shown in Fig. 6, several successive stages were observed during the warmup/cooldown CCDW–TCDW phase transitions: a SCDW state above ~ 160 K, a NCDW state above ~ 180 K during the warmup process, a BTCDW state below ~ 230 K, a NCDW state below ~ 200 K, and finally a MCDW state below ~ 160 K during cooldown from the TCDW phase. These emergent electronic states within the CCDW/TCDW phase can be phenomenologically attributed to the competition and/or cooperation of diverse interactions, including stacking-dependent interlayer interactions, intralayer electron-electron correlations, and e - ph coupling of $1T$ -TaS₂.

As shown in Fig. 6, the SCDW state and NCDW state emerge spontaneously at a temperature of ~ 160 K– 230 K, and disappear completely at a temperature below ~ 160 K. We suggest that the emergence of the SCDW state and NCDW state is related to the vanishing of interlayer stacking order and the dominance role of electron-electron correlations, which is consistent with the recent ARPES experiments and theoretical calculations [22,25]. The temperature-dependent ARPES measurements [25] indicated that the electron-electron correlations play a more dominating role than the interlayer interactions at a temperature of 175 – 225 K. The Monte Carlo (MC) simulations [22] showed that above ~ 200 K, the CDW stacking order is rather random with many unstable stacking interfaces, and as the temperature goes below ~ 120 K, the CDW stacking order is restabilized. At temperatures above ~ 230 K, $1T$ -TaS₂ transforms from the CCDW phase to the stripelike TCDW phase. The phase transition of CCDW–TCDW is widely considered to be a first-order phase transition [5], originating from the significant role played by the interplay of electron-electron correlations and e - ph coupling of $1T$ -TaS₂. As a result of direct cooldown from the TCDW phase, the BTCDW state split from the TCDW region. The TCDW belts are arranged in parallel at fixed intervals along the atomic lattice direction, reflecting the delicate competition of electron-electron and e - ph coupling of $1T$ -TaS₂. At temperatures below ~ 160 K, the NCDW state completely transforms

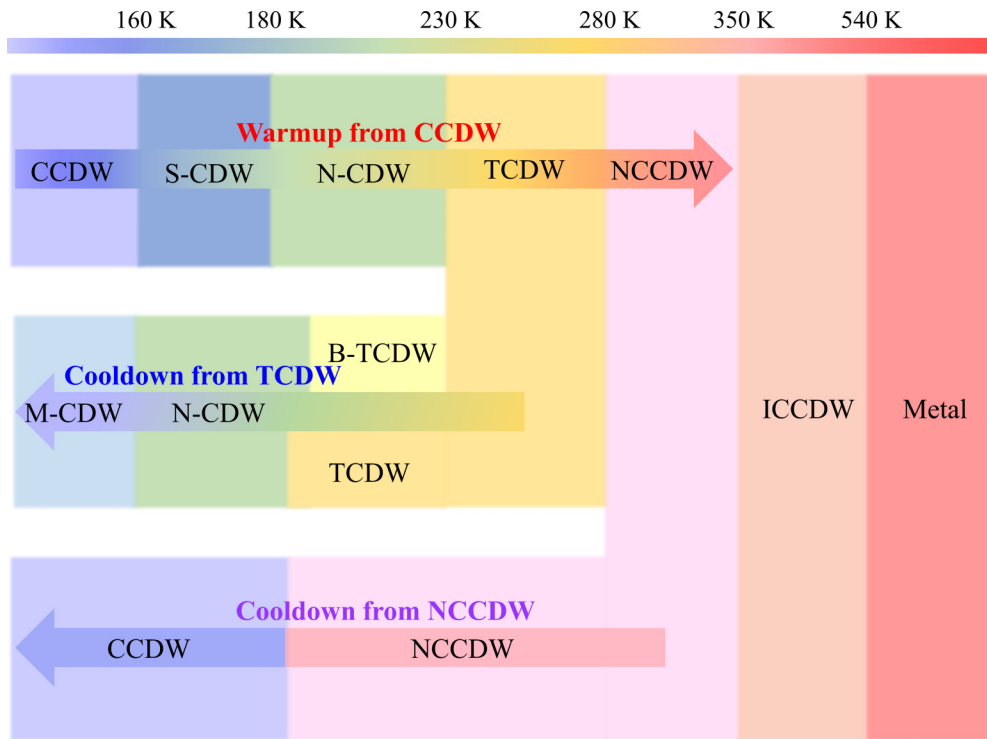


FIG. 6. Schematic of the CDW phases as a function of temperature during the warmup/cooldown process of $1T$ -TaS₂. The bulk $1T$ -TaS₂ undergoes a series of CDW transitions upon warmup, a SCDW state at ~ 160 K, a NCDW state at ~ 180 K, a TCDW phase at ~ 230 K, and a NCCDW phase at ~ 280 K as shown in the top arrow. Cooldown from the NCCDW phase; $1T$ -TaS₂ transforms directly from the NCCDW phase to the CCDW phase at ~ 180 K as shown in the bottom arrow, which most previous studies have focused on [28–30]. In this paper, we mainly focus on the TCDW-CCDW phase transition process as shown in the middle arrow, which is completely different from the NCCDW-CCDW phase transition. Owing to the more delicate competition of various interactions of $1T$ -TaS₂, the more exotic electronic states emerged within the TCDW phase. Upon cooldown, $1T$ -TaS₂ enters a BTCDW state below ~ 230 K, a NCDW state below ~ 200 K, and then a MCDW state below ~ 160 K.

to the MCDW state, which the stacking-dependent interlayer interactions redominate.

Based on the above discussion, we believe that more exotic electronic states can be realized by further accurately and efficiently controlling the various complex interactions of $1T$ -TaS₂. In our subsequent work, a unique electronic Kagome lattice [35] can be obtained at ~ 200 K in $1T$ -TaS₂ by modifying the interplay of e - ph coupling and electron-electron correlations, and we can further control the competition between the interlayer interactions and intralayer electron-electron correlations through Ti or W-doped $1T$ -TaS₂ to realize exotic electronic states. A very small amount of W-doped $1T$ -TaS₂ effectively modifies the intralayer electron-electron correlations by increasing the number of intralayer electrons, reproducing the same correlated SCDW and NCDW states of pristine $1T$ -TaS₂ at low temperatures, which can be considered as a representative electron correlation system. However, Ti-doped $1T$ -TaS₂ cannot reproduce the same correlated SCDW and NCDW states of pristine $1T$ -TaS₂ at low/high temperatures by decreasing the number of intralayer electrons. These results provide a site to search for strongly correlated phenomena and exotic

electronic states by precisely controlling various interactions in two-dimensional (2D) correlated materials.

IV. CONCLUSION

In summary, VTSTM measurements were performed to investigate the spatially hysteretic electronic phase transitions in the correlated CDW state of $1T$ -TaS₂. The dynamic behaviors of SCDW, NCDW, BTCDW, and MCDW states within the CCDW/TCDW phase were detailed studied at the atomic scale and mesoscopic scale through a warmup and cooldown process. We further discuss the effect of competition and/or cooperation between the various interactions on the emergent electronic states of $1T$ -TaS₂. Deeply understanding the delicate competition and accurately regulating the various interactions of $1T$ -TaS₂ will motivate more research to find the exotic electronic states in the low-dimensional materials.

V. MATERIALS AND METHODS

High-quality $1T$ -TaS₂ single crystals supplied by HQ Graphene were grown using the chemical vapor transport (CVT) method with iodine as a transport agent. The samples

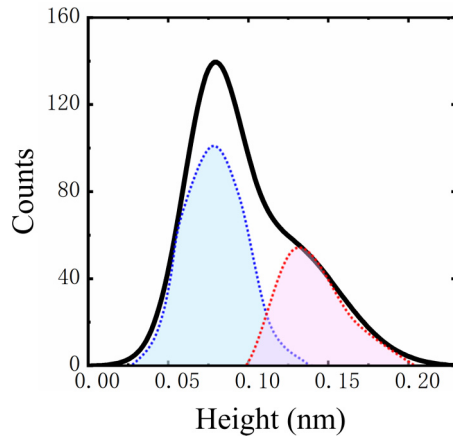


FIG. 7. Height distribution curves of the SCDW state. Height distribution curves of bright clusters and pristine SDs of the SCDW state are marked by the red and blue dotted lines, respectively. The apparent heights of the bright clusters are ~ 50 pm higher than the remaining pristine SDs of the SCDW state. The bright clusters account for $\sim 20\%$ of the entire SCDW state.

were cleaved at room temperature under ultrahigh-vacuum conditions at a base pressure of 2×10^{-10} Torr and quickly transferred to the variable-temperature STM system (PanScan

Freedom, RHK, USA). The variable-temperature STM measurements were performed using liquid-He-free cryocooler technology with adjustable heating power at the cold head. Chemically etched tungsten tips were used for constant-current STM measurements. The tips were prepared and calibrated on a clean Ag (111) (MaTeck, Germany) surface, which was cleaned by repeated cycles of argon ion sputtering and annealing at 550 K. The STM measurements were mostly performed in the hysteresis temperature range of 1T-TaS₂, and the investigation of the three phases, i.e., CCDW, TCDW, and NCCDW, were investigated via precise regulation of the temperature. STS measurements were also performed at high temperatures (~ 160 K), which was challenging owing to the thermal-broadening effect. The STM data were analyzed and processed with GWYDDION software.

ACKNOWLEDGMENTS

This project is supported by the National Natural Science Foundation of China (NSFC) (Grants No. 21622304, No. 61674045, and No. 11604063) and the Strategic Priority Research Program (Chinese Academy of Sciences, CAS) (Grant No. XDB30000000). Z.C. was supported by the Fundamental Research Funds for the Central Universities and the Research Funds of Renmin University of China (No. 21XNLG27).

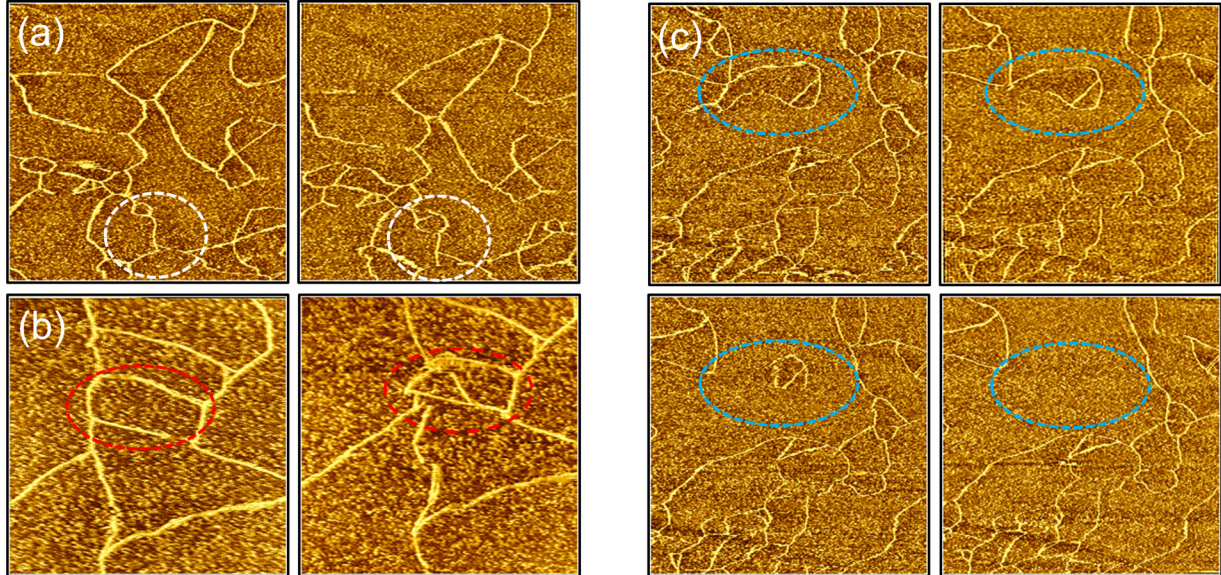


FIG. 8. Emergent bright stripes with dynamic behaviors within the NCDW state. (a) Mesoscopic-scale STM image of bright stripes with the behavior of breaking marked by the white dashed circles. (b) Mesoscopic-scale STM image of bright stripes with the behavior of shrinking marked by the red dashed circles. (c) Mesoscopic-scale STM image of isolated stripe loops with the behavior of breaking, shrinking, and disappearing marked by the blue dashed circles. Imaging parameters: $1.5 \times 1.5 \text{ um}^2$. $V_b = -100 \text{ mV}$, $I_t = -100 \text{ pA}$ (a), (b); $2 \times 2 \text{ um}^2$. $V_b = -150 \text{ mV}$, $I_t = -150 \text{ pA}$ (c).

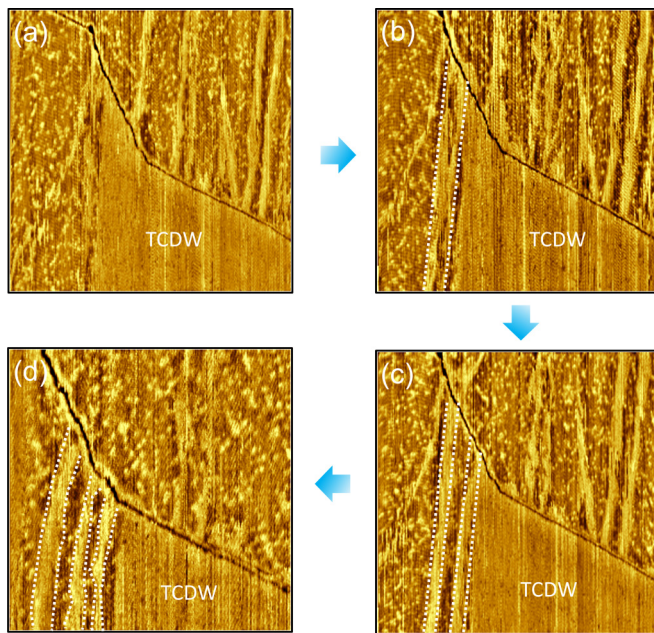


FIG. 9. Formation process of the BTCDW state. (a)–(d) Large-scale STM image of the emergent bright belts decomposed from the TCDW phase. The blue arrow indicates the split process of the bright belts. The white dashed line indicates the emergent bright belts. Imaging parameters: $350 \times 350 \text{ nm}^2$. $V_b = -200 \text{ mV}$, $I_t = -100 \text{ pA}$ (a)–(d).

APPENDIX A: SCDW STATE AND NCDW STATE OF $1T\text{-TaS}_2$ DURING WARMUP PROCESS

The Fig. 7 show the height distribution of SCDW state. The bright clusters of SCDW normally consist of approximately five to eight bright SDs. The bright clusters account for $\sim 20\%$

of the entire SCDW state. The apparent heights of the bright clusters are $\sim 50 \text{ pm}$ higher than that of the remaining pristine SDs of the SCDW state.

Figure 8 shows the dynamic behavior of the bright stripes within the NCDW state. The evolution of the global bright stripe network with scanning is indicated by the dashed circles in Fig. 8, showing the breaking, shrinking, and disappearing dynamic behaviors. The relatively large bright stripe network can be gradually shrunk into a small bright stripe network, and a smaller bright stripe network can also become a larger bright stripe network through the disappearance of certain bright stripes. The isolated stripe loops can be decomposed from the large bright stripe network and retain a specific topological stability relative to the unstable global bright stripe network.

APPENDIX B: BTCDW STATE OF $1T\text{-TaS}_2$ DURING COOLDOWN PROCESS

As a result of the direct cooldown from the TCDW phase, the TCDW phase gradually split- decomposes into bright belts, forming a belt-TCDW (BTCDW) state. The initial stage of the BTCDW state as shown in Fig. 9, with the bright belts splitting out of the TCDW phase one by one. The bright belts are arranged in parallel and the bright clusters have reemerged between the bright TCDW belts.

STS of BTCDW state was also performed, and only similar rough “V-shaped” features were observed, which were attributed to the thermal-broadening effect at $\sim 200 \text{ K}$. At temperatures below $\sim 160 \text{ K}$, the NCDW state completely transforms into the global mosaic-CDW (MCDW) state; STS shows the small gap features reemerged, Fig. 10.

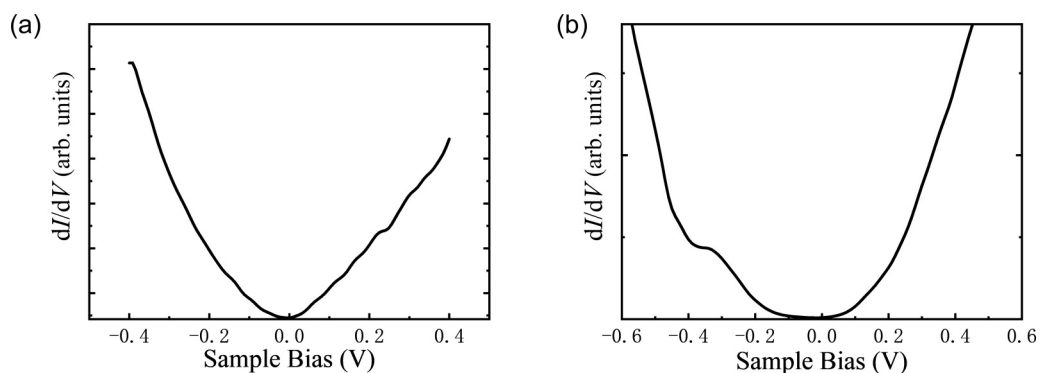


FIG. 10. Representative dI/dV spectroscopy acquired at different temperatures. (a) The STS was also performed at temperatures above $\sim 200 \text{ K}$, and only the similar rough “V-shaped” features were observed at the TCDW region and BTCDW region. (b) STS was also performed at temperatures below $\sim 160 \text{ K}$; STS shows the small gap features reemerged at the MCDW region.

- [1] C. S. Lian, C. Si, and W. H. Duan, Unveiling charge-density wave, superconductivity, and their competitive nature in two-dimensional NbSe₂, *Nano Lett.* **18**, 2924 (2018).
- [2] F. H. Yu, D. H. Ma, W. Z. Zhuo, S. Q. Liu, X. K. Wen, B. Lei, and X. H. Chen, Unusual competition of superconductivity and charge-density-wave state in a compressed topological kagome metal, *Nat. Commun.* **12**, 3645 (2021).
- [3] L. P. Nie, K. Sun, W. R. Ma, D. W. Song, L. X. Zheng, Z. W. Liang, P. Wu, F. H. Yu, J. Li, M. Shan, D. Zhao, S. J. Li, B. L. Kang, Z. M. Wu, Y. B. Zhou, K. Liu, Z. J. Xiang, J. J. Ying, Z. Y. Wang, T. Wu *et al.*, Charge-density-wave-driven electronic nematicity in a kagome superconductor, *Nature (London)* **604**, 59 (2022).
- [4] R. E. Thorne, Charge-density-wave conductors, *Phys. Today* **49**(5), 42 (1996).
- [5] K. Rossnagel, On the origin of charge-density waves in select layered transition-metal dichalcogenides, *J. Phys.: Condens. Matter* **23**, 213001 (2011).
- [6] F. Clerc, C. Battaglia, M. Bovet, L. Despont, C. Monney, H. Cercellier, M. Garnier, P. Aebi, H. Berger, and L. Forró, Lattice-distortion-enhanced electron-phonon coupling and Fermi surface nesting in 1T-TaS₂, *Phys. Rev. B* **74**, 155114 (2006).
- [7] A. Y. Liu, Electron-phonon coupling in compressed 1T-TaS₂: Stability and superconductivity from first principles, *Phys. Rev. B* **79**, 220515(R) (2009).
- [8] K. Lasek, J. F. Li, S. Kolekar, P. M. Coelho, L. Guo, M. Zhang, Z. M. Wang, and M. Batzill, Synthesis and characterization of 2D transition metal dichalcogenides: Recent progress from a vacuum surface science perspective, *Surf. Sci. Rep.* **76**, 100523 (2021).
- [9] M. M. Ugeda, A. J. Bradley, Y. Zhang, S. Onishi, Y. Chen, W. Ruan, C. Ojeda-Aristizabal, H. Ryu, M. T. Edmonds, H. Z. Tsai, A. Riss, S. K. Mo, D. Lee, A. Zettl, Z. Hussain, Z. X. Shen, and M. F. Crommie, Characterization of collective ground states in single-layer NbSe₂, *Nat. Phys.* **12**, 92 (2016).
- [10] P. Chen, Y. H. Chan, M. H. Wong, X. Y. Fang, M. Y. Chou, S. K. Mo, Z. Hussain, A. V. Fedorov, and T. C. Chiang, Dimensional effects on the charge density waves in ultrathin films of TiSe₂, *Nano Lett.* **16**, 6331 (2016).
- [11] Y. Chen, W. Ruan, M. Wu, S. Tang, H. Ryu, H. Z. Tsai, R. Lee, S. Kahn, F. Liou, C. Jia, O. R. Albertini, H. Xiong, T. Jia, Z. Liu, J. A. Sobota, A. Y. Liu, J. E. Moore, Z.-X. Shen, S. G. Louie, S.-K. Mo *et al.*, Strong correlations and orbital texture in single-layer 1T-TaS₂, *Nat. Phys.* **16**, 218 (2020).
- [12] Y. Nakata, K. Sugawara, A. Chainani, H. Oka, C. Bao, S. Zhou, P. Y. Chuang, C. M. Cheng, T. Kawakami, Y. Saruta, T. Fukumura, S. Zhou, T. Takahashi, and T. Sato, Robust charge-density wave strengthened by electron-electron correlations in monolayer 1T-TaSe₂ and 1T-NbSe₂, *Nat. Commun.* **12**, 5873 (2021).
- [13] B. Sipos, A. F. Kusmartseva, A. Akrap, H. Berger, L. Forro, and E. Tutis, From Mott state to superconductivity in 1T-TaS₂, *Nat. Mater.* **7**, 960 (2008).
- [14] L. J. Li, W. J. Lu, X. D. Zhu, L. S. Ling, Z. Qu, and Y. P. Sun, Fedoping-induced superconductivity in the charge-density-wave system 1T-TaS₂, *EPL* **97**, 67005 (2012).
- [15] Y. J. Yu, F. Y. Yang, X. F. Lu, Y. J. Yan, Y. H. Cho, L. G. Ma, X. H. Niu, S. Kim, Y. W. Son, D. L. Feng, S. Y. Li, S. W. Cheong, X. H. Chen, and Y. B. Zhang, Gate-tunable phase transitions in thin flakes of 1T-TaS₂, *Nat. Nanotechnol.* **10**, 270 (2015).
- [16] Y. Liu, D. F. Shao, L. J. Li, W. J. Lu, X. D. Zhu, P. Tong, R. C. Xiao, L. S. Ling, C. Y. Xi, L. Pi, H. F. Tian, H. X. Yang, J. Q. Li, W. H. Song, X. B. Zhu, and P. Y. Sun, Nature of charge density waves and superconductivity in 1T-TaSe_{2-x}Te_x, *Phys. Rev. B* **94**, 045131 (2016).
- [17] W. Zhang, D. Ding, J. Gao, K. Bu, Z. Wu, L. Wang, F. Li, W. Wang, X. Luo, W. Lu, C. Jin, Y. Sun, and Y. Yin, Modulation of electronic state in copper-intercalated 1T-TaS₂, *Nano Res.* **15**, 4327 (2022).
- [18] J. A. Wilson, F. Di Salvo, and S. Mahajan, Charge-density waves and superlattices in the metallic layered transition metal dichalcogenides, *Adv. Phys.* **24**, 117 (1975).
- [19] K. T. Law and P. A. Lee, 1T-TaS₂ as a quantum spin liquid, *Proc. Natl. Acad. Sci. USA* **114**, 6996 (2017).
- [20] J. J. Kim, W. Yamaguchi, T. Hasegawa, and K. Kitazawa, Observation of Mott Localization Gap Using Low Temperature Scanning Tunneling Spectroscopy in Commensurate 1T-TaS₂, *Phys. Rev. Lett.* **73**, 2103 (1994).
- [21] C. J. Butler, M. Yoshida, T. Hanaguri, and Y. Iwasa, Mottness versus unit-cell doubling as the driver of the insulating state in 1T-TaS₂, *Nat. Commun.* **11**, 2477 (2020).
- [22] S. H. Lee, J. S. Goh, and D. Cho, Origin of the Insulating Phase and First-Order Metal-Insulator Transition in 1T-TaS₂, *Phys. Rev. Lett.* **122**, 106404 (2019).
- [23] T. Ritschel, H. Berger, and J. Geck, Stacking-driven gap formation in layered 1T-TaS₂, *Phys. Rev. B* **98**, 195134 (2018).
- [24] J. Lee, K. H. Jin, and H. W. Yeom, Distinguishing a Mott Insulator from a Trivial Insulator with Atomic Adsorbates, *Phys. Rev. Lett.* **126**, 196405 (2021).
- [25] Y. D. Wang, W. L. Yao, Z. M. Xin, T. T. Han, Z. G. Wang, L. Chen, C. Cai, Y. Li, and Y. Zhang, Band insulator to Mott insulator transition in 1T-TaS₂, *Nat. Commun.* **11**, 4215 (2020).
- [26] L. Perfetti, T. A. Gloor, F. Mila, H. Berger, and M. Grioni, Unexpected periodicity in the quasi-two-dimensional Mott insulator 1T-TaS₂ revealed by angle-resolved photoemission, *Phys. Rev. B* **71**, 153101 (2005).
- [27] L. Stojchevska, I. Vaskivskiy, T. Mertelj, P. Kusar, D. Svetin, S. Brazovskii, and D. Mihailovic, Ultrafast stable hidden quantum state in an electronic crystal, *Science* **344**, 177 (2014).
- [28] J. W. Park, G. Y. Cho, J. Lee, and H. W. Yeom, Emergent honeycomb network of topological excitations in correlated charge density wave, *Nat. Commun.* **10**, 4038 (2019).
- [29] K. Ludwiczak, E. Lacinska, J. Binder, I. Lutsyk, M. Rogala, P. Dabrowski, Z. Klusek, R. Stepniowski, and A. Wyszomolek, Impeded phase transition in 1T-TaS₂: Thermoelectric fingerprint of long-lived mixed states, *Solid State Commun.* **305**, 113749 (2020).
- [30] S. W. Shen, B. Shao, C. H. Wen, X. Q. Yuan, J. J. Gao, Z. W. Nie, X. Luo, B. Huang, Y. P. Sun, S. Meng, and S. C. Yan, Single-water-dipole-layer-driven reversible charge order transition in 1T-TaS₂, *Nano Lett.* **20**, 8854 (2020).
- [31] W. Wang, D. Dietzel, and A. Schirmeisen, Lattice discontinuities of 1T-TaS₂ across first order charge density wave phase transitions, *Sci. Rep.* **9**, 7066 (2019).
- [32] L. Ma, C. Ye, Y. Yu, X. F. Lu, X. Niu, S. Kim, D. Feng, D. Tomanek, Y. W. Son, X. H. Chen, and Y. Zhang, A metallic mo-

- saic phase and the origin of Mott-insulating state in $1T$ -TaS₂, [Nat. Commun. 7, 10956 \(2016\)](#).
- [33] D. Cho, S. Cheon, K. S. Kim, S. H. Lee, Y. H. Cho, S. W. Cheong, and H. W. Yeom, Nanoscale manipulation of the Mott insulating state coupled to charge order in $1T$ -TaS₂, [Nat. Commun. 7, 10453 \(2016\)](#).
- [34] S. M. Walker, T. Patel, J. Okamoto, D. Langenberg, E. A. Bergeron, J. Gao, X. Luo, W. Lu, Y. Sun, A. W. Tsen, and J. Baugh, Observation and manipulation of a phase separated state in a charge density wave material, [Nano. Lett. 22, 1929 \(2022\)](#).
- [35] H. Y. Dong, P. H. Sun, L. Lei, Y. Y. Geng, J. F. Guo, Y. Li, L. Huang, R. Xu, F. Pang, W. Ji, W. C. Zhou, Z. Liu, Z. Y. Lu, H. J. Gao, K. Liu, and Z. H. Cheng, Emergent electron-based kagome lattice in correlated charge–density–wave state of $1T$ -TaS₂, [arXiv:2301.05885 \[cond-mat.mtrl-sci\] \(2023\)](#).